Highly confined low-loss plasmons in graphene–boron nitride heterostructures

Achim Woessner[1†], Mark B. Lundeberg[1†], Yuanda Gao[2†], Alessandro Principi[3], Pablo Alonso-González[4], Matteo Carrega[5,6], Kenji Watanabe[7], Takashi Taniguchi[7], Giovanni Vignale[3], Marco Polini[5,8], James Hone[2], Rainer Hillenbrand[9,10] and Frank H. L. Koppens[1*]

Graphene plasmons were predicted to possess simultaneous ultrastrong field confinement and very low damping, enabling new classes of devices for deep-subwavelength metamaterials, single-photon nonlinearities, extraordinarily strong light–matter interactions and nano-optoelectronic switches. Although all of these great prospects require low damping, thus far strong plasmon damping has been observed, with both impurity scattering and many-body effects in graphene proposed as possible explanations. With the advent of van der Waals heterostructures, new methods have been developed to integrate graphene with other atomically flat materials. In this Article we exploit near-field microscopy to image propagating plasmons in high-quality graphene encapsulated between two films of hexagonal boron nitride (h-BN). We determine the dispersion and plasmon damping in real space. We find unprecedentedly low plasmon damping combined with strong field confinement and confirm the high uniformity of this plasmonic medium. The main damping channels are attributed to intrinsic thermal phonons in the graphene and dielectric losses in the h-BN. The observation and in-depth understanding of low plasmon damping is the key to the development of graphene nanophotonic and nano-optoelectronic devices.

Graphene–h-BN heterostructures[1,2] have recently attracted great interest owing to their unusual electronic band structure, sensitive to the crystallographic alignment between graphene and h-BN (ref. 3). Optically, these heterostructures are just beginning to be explored[4], and they are expected to produce unusual plasmonic behaviour in the case of an aligned lattice[5]. Furthermore, h-BN itself is an interesting optical material as it shows natural hyperbolic behaviour, meaning that the in- and out-of-plane component of the permittivity have opposite signs in the reststrahlen frequency bands[6]. This implies that h-BN supports deep subwavelength slow-light phonon polariton modes within those bands[7,8]. Combining h-BN with graphene gives rise to unconventional plasmon–phonon hybridization[4] and this hybrid system can be used for tailoring novel subwavelength metamaterials[9–21]. Besides all of those exotic properties, h-BN can provide an exceptionally clean environment for graphene. Recent advances in graphene device fabrication, exploiting the unique properties of h-BN heterostructures produced by the polymer-free van der Waals assembly technique, have resulted in significantly less disorder. This leads to the carrier transport mobility at room temperature reaching its intrinsic limit dominated by thermal phonon scattering[22].

Here we demonstrate that in this new type of heterostructure, sketched in Fig. 1a, marked improvements in the graphene plasmon damping and field confinement can be achieved. Furthermore, we establish an excellent understanding of the graphene plasmon dispersion and damping for a wide range of carrier densities. In contrast to earlier reports[23,24], we find much lower plasmon damping and that impurity scattering does not play a significant role in plasmon damping, thus indicating very low intrinsic limits on the plasmon damping in graphene. This shows that graphene encapsulated in h-BN provides an excellent platform for graphene plasmonic devices.

A topographic image of the device is depicted in Fig. 1b. The h-BN (7 nm)–graphene–h-BN (46 nm) stack assembled by the polymer-free van der Waals assembly technique[22] lies on top of an oxidized silicon wafer, used as a backgate. This stack is etched into a triangle and is electrically side-contacted with metal electrodes[22].

We image propagating plasmons with a scattering-type scanning near-field optical microscope[25,26] (s-SNOM), similar to several recent studies of graphene plasmons[23,24,27–31]. A schematic of the s-SNOM interacting with the graphene device is shown in Fig. 1c. A continuous wave laser, with tunable photon energy from 115 to 135 meV (laser wavelength λ_0 from 10.8 to 9.2 μm), is focused on a metallized atomic force microscope probe tip. With this laser we operate in the highly birefringent spectral region between the two reststrahlen bands, where the plasmon damping is predicted to be low[32]. The tip apex optically couples to the device in the near field. The sharpness of the apex provides wavevector matching between plasmons and incident photons[33]. The incident light is partly converted to plasmons, which propagate away from the tip as a circular wave with complex wavevector q_p. Plasmons return to the tip if they are reflected by edges or defects. Returning plasmons are partly converted to light and add to the out-scattered light field. Interferometric detection of the scattered light yields the magnitude and phase of the complex-valued optical signal ξ_{opt}. A scan of $\text{Re}\,\xi_{opt}$ versus tip position near the graphene edge shows characteristic fringes owing to the varying field of the reflected
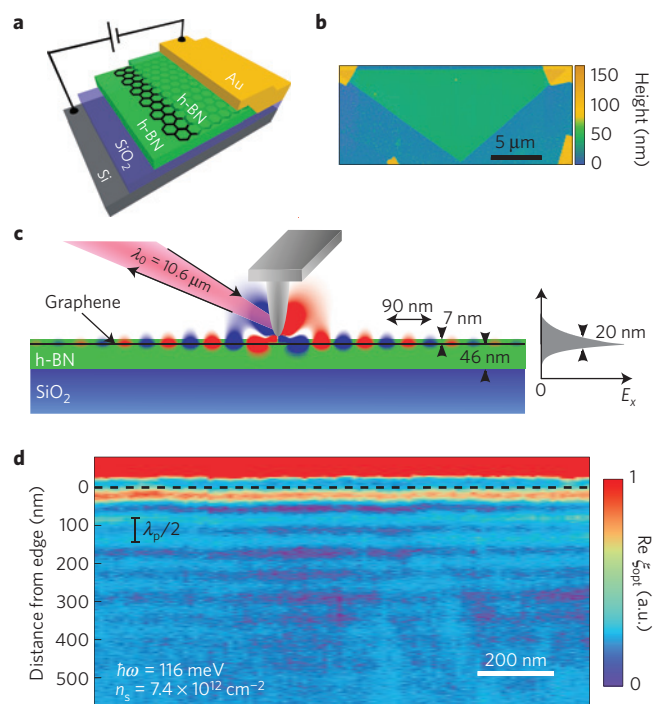
Figure 1 | Device and plasmon imaging with s-SNOM. a, Sketch of the layered heterostructure with a Si backgate, SiO_2 layer, h-BN, graphene, h-BN and a gold side contact. **b**, Topographic image of the device. The triangle shows two h-BN layers encapsulating a graphene layer, contacted at two corners. The blue outer area is etched. **c**, Simplified side-view schematic of the s-SNOM measurement, including probe tip, excitation (with laser source of wavelength λ_0) and detection. Plasmons are launched radially from the tip. The red and blue shows the simulated in-plane component of the electric field of a dipole source oscillating at a photon energy of 116 meV coupling to graphene plasmons. The simulated field confinement in the x direction (E_x) of the plasmon in the out-of-plane direction of 20 nm full-width at half-maximum can be seen on the right. **d**, s-SNOM optical signal from a two-dimensional scan of the tip position, near the graphene edge (dashed line) at room temperature. Edge-reflected plasmons appear as interference fringes.

Figure 2 | Optical signal and plasmon wavelength dependence on carrier density and photon energy. a, s-SNOM optical signal, Re ξ_{opt}, from a scan of tip position perpendicular to the graphene edge (dashed line) and gate voltage, showing the gate dependence of plasmon fringes at a photon energy of $\hbar\omega = 116$ meV. **b**, Change in complex optical signal away from the edge (blue, from **a**) with respect to the gate voltage compared with the theoretical local conductivity for ideal graphene (red)[48,49]. **c**, Plasmon wavelength dependence on carrier density. **d**, Frequency dependence of the plasmon, at $n_s = 7.4 \times 10^{12}$ cm^{-2}. Shaded orange regions indicate the h-BN frequency bands in which propagating phonon polaritons can exist. In both **c** and **d**, crosses show the extracted experimental values and the red background colour shows the imaginary part of the Fresnel reflection coefficient (see Methods). The electronic intraband Landau damping region is shaded green.

plasmon, interfering with the local response[23,24]. Figure 1c shows these fringes measured near a straight edge in our device. Because the plasmon returns to the tip after travelling twice the tip–edge distance, the spacing between fringes is $\lambda_p/2$, where $\lambda_p = 2\pi/\mathrm{Re}\,q_p$ is the plasmon wavelength[23,24].

Owing to the encapsulation of the graphene, our device possesses only small intrinsic doping and a uniform doping distribution with a small density of electron–hole puddles[34]. This enables us to study the optical response for a wide range of carrier densities n_s, including features near the charge neutrality point, by applying a backgate voltage V_g. In Fig. 2a we tune the plasmon fringes in both wavelength and amplitude and show that λ_p depends strongly on n_s. With decreasing carrier density the fringe visibility decreases, as the wavelength of plasmons becomes shorter. The tip cannot couple to plasmons with an arbitrarily short wavelength owing to the non-zero tip radius[33] and their confinement in the top h-BN layer.

While changing n_s we also observe changes in the local optical response. This is most clearly seen in Fig. 2b, where we plot ξ_{opt} versus n_s with the signal averaged from 400 nm to 700 nm from the edge, where plasmon interference effects are weak. With an appropriately chosen phase, ξ_{opt} is approximately proportional to the change in complex-valued graphene conductivity σ (Fig. 2b
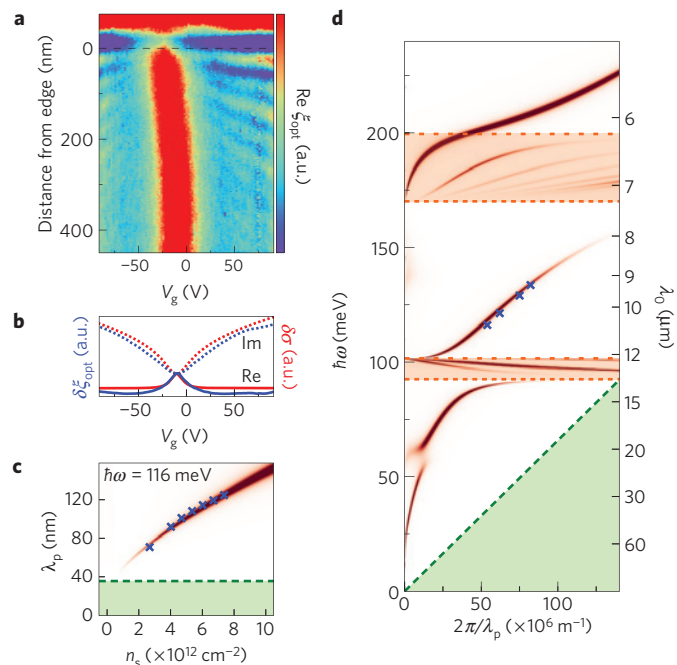
and see Supplementary Information). Near charge neutrality (small $|n_s|$), Re σ dominates, which gives information about interband conductivity. A corresponding peak in Re ξ_{opt} appears where graphene is charge neutral, in this case near $V_g \approx -10$ V. With increasing carrier density, Re σ (Re ξ_{opt}) decreases as a result of Pauli blocking and Im σ (Im ξ_{opt}) grows as a result of ballistic free-carrier motion (Drude-like response). With this technique we confirm the spatial uniformity of the position of the graphene charge neutrality point and deduce that plasmons are hosted in graphene with uniform carrier density.

A detailed study of the plasmon wavelength dependence on carrier density and frequency is shown in Fig. 2c,d, together with calculations of the graphene plasmon dispersion of the full system. The calculations include optical thin-film effects which need to be included owing to the thin h-BN top film, as well as graphene nonlocal conductivity, which needs to be considered owing to the low plasmon phase velocity (Supplementary Information). The measured wavelengths show parameter-free agreement with these electromagnetic calculations (red curves in Fig. 2c,d; details in Methods). The extra modes (in the orange bands in Fig. 2d) that appear in the calculation are due to the propagating phonon polaritons in thin h-BN (refs 7,8). These phonon modes can hybridize with the graphene plasmons; however, the plasmons are effectively unhybridized for the frequency range used in this study.
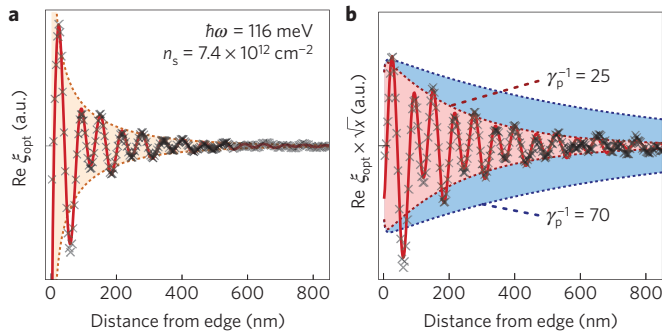
Figure 3 | Extraction of plasmon damping. a, Black crosses show the s-SNOM optical signal from Fig. 1d, averaged along the edge, with a smooth background subtracted. A fit to equation (1) is shown as a red line. The shaded region shows the decay envelope of the first term of equation (1). **b**, Same signal and fit as in **a**, multiplied by $\sqrt{x}$ to isolate exponential decay. The shaded regions show the exponential decay envelopes of the first term of equation (1) for the measured damping ($\gamma_p^{-1}=25$) and for the case limited only by electron scattering from thermal phonons ($\gamma_p^{-1}=70$).
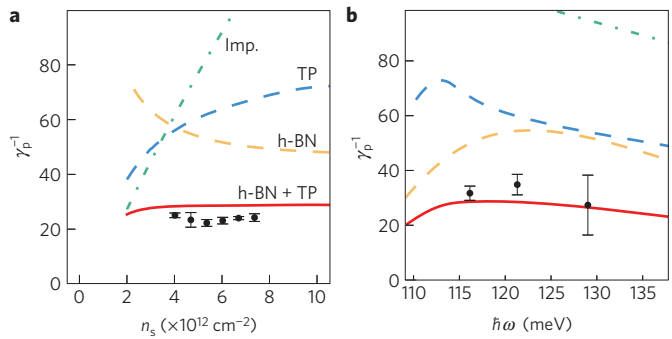

Figure 4 | Plasmon damping mechanisms. a, Inverse damping ratio as a function of carrier density at a photon energy of 116 meV. **b**, Inverse damping ratio as a function of excitation frequency at a carrier density of 7.4×10^{12} cm^{-2}. Both **a,b** also show the theoretical inverse damping ratios due to graphene thermal phonons (blue dashed curve), charge impurities at concentration $n_{imp} = 1.9 \times 10^{11}$ cm^{-2} (green dash-dotted curve), dielectric losses of h-BN (yellow dashed curve) and the combination of graphene thermal phonons and dielectric losses of h-BN (red curve). The error bars represent the 95% confidence intervals.

For our frequency range, the h-BN lattice is nonresonant yet yields a highly anisotropic dielectric—that is, birefringent—environment for the plasmon, which enhances its confinement. The out-of-plane full-width at half-maximum confinement of the plasmon electric field is calculated to be ~20 nm (Fig. 1c). We observe λ_p as low as 70 nm, which is 150 times smaller than the free-space light wavelength. This constitutes a record high volume confinement of propagating optical fields of ~10^7 compared to the modal volume in free space.

The capability to carry plasmons with such strong field confinement and at the same time relatively low propagation damping is a unique property of graphene compared to other plasmonic materials[9]. To quantify the propagation damping, we average linescans of the complex ξ_{opt} perpendicular to the graphene edge at different locations, and subtract the background (Fig. 3a). The decay of the fringes away from an edge is due to a combination of damping (Im $q_p > 0$) and circular-wave geometrical spreading. The oscillating signal of Fig. 3a is fitted well with

$$\xi_{opt}(x) = A\frac{e^{i2q_p x}}{\sqrt{x}} + B\frac{e^{iq_p x}}{x^a} \qquad (1)$$

with complex parameters A, B, q_p and real a. The first term is the returning field for a damped circular wave reflected from a straight edge, with the plasmon travelling a distance $2x$. The second term interferes with the first, producing alternating fringe amplitudes. It arises because plasmons are not only generated/detected beneath the tip apex, but also weakly at the edge of the graphene[35]. These plasmons travel only the tip–edge distance x and therefore show twice the fringe spacing of the plasmons generated/detected beneath the tip apex. As the geometrical decay of the plasmon travelling the tip–edge distance only once is not known a priori, we allow for a variable decay $a \sim 1$. Nevertheless, because the $\exp(2iq_p x)$ component dominates and we can separate the $\exp(iq_p x)$ component with Fourier analysis, we can extract Im q_p unambiguously (Supplementary Information).

We define the inverse damping ratio $\gamma_p^{-1} =$ Re q_p/ Im q_p as a dimensionless figure of merit of propagation damping. Figure 3b shows the data multiplied by $\sqrt{x}$ to isolate the damping decay $\exp(-2\,\mathrm{Im}\,q_p x)$, and visually indicates the significance of γ_p^{-1}—in this case, $\gamma_p^{-1} \approx 25$. This is a significant improvement over the $\gamma_p^{-1} \sim 5$ seen in studies of unencapsulated graphene on silicon dioxide[23,24].

From spatial damping, the plasmon amplitude decay time τ_p can be calculated using the group velocity $v_g = (\mathrm{d}\,\mathrm{Re}\,q_p/\mathrm{d}\omega)^{-1}$. In this case $v_g \approx 10^6$ m s^{-1}, coincidentally the same as the Fermi velocity of graphene electrons (Fig. 2d). We find $\tau_p = (\mathrm{Im}\,q_p)^{-1}/v_g \approx 500$ fs, which is remarkably long for strongly confined optical fields, and an order of magnitude longer than the amplitude decay time of plasmons in silver, the metal with the longest plasmon amplitude decay time[36]. For surface plasmons at a Ag/SiO$_2$ interface, inverse damping ratios above 20 are feasible only for an energy range where the wavelength confinement is below two[9].

Plasmon damping can arise from a number of mechanisms, most of which involve electron scattering. Electrons can scatter from the disorder potential in the graphene, created by extrinsic charge impurities[37] and the intrinsic thermal phonons[32]. Electrons may also inelastically scatter by absorbing energy from the plasmon while emitting an optical phonon in the graphene or in the substrate[9,15,32]. Coherent many-electron scattering processes have been calculated to play a minor role[38]. Besides dissipating energy electronically, plasmons also dissipate via dielectric losses in the environment, for example, through direct heating of the substrate[32,37].

We investigate the role of the different damping mechanisms by measuring the inverse damping ratio as a function of both n_s and excitation frequency, and compare the results in Fig. 4 with the calculated damping for various damping channels. The calculations are based on the nonlocal conductivity $\sigma(q, \omega)$ evaluated at a plasmon wavevector $q = q_p$ and excitation frequency ω. These calculations show that charge carrier scattering is strongly modified at high frequency and thus the effective electron scattering time for plasmons can differ from the transport scattering time[32,37].

Interestingly, we find experimentally that plasmon damping is not affected by the carrier density. By comparing our data with the calculated inverse damping ratios, we find that impurity scattering does not play a role for plasmon damping in these high-quality heterostructures, because it would lead to strongly reduced damping for increasing n_s, owing to increasing electrostatic screening[37]. This trend is shown by the green dash-dotted curve in Fig. 4 which is based on a plasmon damping theory due to impurity scattering[37]. In contrast, plasmon damping by intrinsic thermal phonons[32] shows a much weaker dependence on n_s (dashed blue curve in Fig. 4). From quantitative comparison, we find that (without fitting parameters) this intrinsic damping mechanism accounts for approximately half the observed damping; thus, we conclude that this is the dominant

intrinsic damping mechanism. Extensive details on the calculations of plasmon damping due to thermal phonon scattering are presented in ref. 32.

Electronic damping alone cannot explain the observed dependences; however, dielectric losses provide an additional damping pathway. In particular, the dielectric losses of the h-BN encapsulating the graphene may give a significant contribution (yellow dashed curve in Fig. 4). The combination of thermal phonon damping and dielectric losses[32] is in good agreement with our measurements (red curve in Fig. 4). The dielectric losses used in our model are consistent with recent measurements of thin (<200 nm) h-BN flakes[8]. Although the plasmon damping is affected by the dielectric losses, this work provides strong evidence of the intrinsic limit inverse damping ratio of 40–70 for graphene plasmons. This provides a upper bound on $\mathrm{Re}\,\sigma \sim 0.05\pi e^2/2h$ at room temperature, much smaller than previously reported[39,40].

To conclude, we have demonstrated h-BN to be an exceptional environment for graphene plasmons, yielding high confinement and low levels of damping. To further reduce damping and reach the ultimate limit of plasmon propagation at room temperature—electron scattering by thermal phonons[32]—it will be necessary to reduce dielectric losses. This should be possible, for example, by improving the quality of thin h-BN films or by increasing the carrier density and exciting plasmons with higher energy further away from the reststrahlen bands of the h-BN. The presented device is ideal for applications where tunability and optical field confinement are crucial, such as for routing of plasmons[41], plasmon lenses[30,42], tunable sensors[43], detectors and light absorbers[44,45], single-plasmon nonlinearities[46] and strong light–matter interactions[12,47].

Methods

The device geometry as well as the edge contacts were defined using electron beam lithography and dry etching, following the method of ref. 22. The backgate capacitance density was estimated to be $6.7 \times 10^{10}\, e\,\mathrm{cm}^{-2}\,\mathrm{V}^{-1}$, where e is the elementary charge.

The s-SNOM used was a NeaSNOM from Neaspec GmbH, equipped with a CO_2 laser and cryogenic HgCdTe detector. The probes were commercially available metallized atomic force microscopy probes with an apex radius of approximately 25 nm. The tip height was modulated at a frequency of approximately 250 kHz with an amplitude of 60–80 nm. ξ_{opt} was obtained from the third harmonic interferometric pseudo-heterodyne signal[23,24]. For simplicity most figures show only $\mathrm{Re}\,\xi_{\mathrm{opt}}$, however, similar information is shown in $\mathrm{Im}\,\xi_{\mathrm{opt}}$ as described by equation (1); all analysis (background subtraction, fitting, and so on) was performed simultaneously on $\mathrm{Re}\,\xi_{\mathrm{opt}}$ and $\mathrm{Im}\,\xi_{\mathrm{opt}}$. The location of the etched graphene edge ($x=0$) was determined from the simultaneously measured topography.

The theoretical model of plasmon modes was calculated using a classical electromagnetic transfer matrix method, with a thin-film stack of vacuum–SiO_2(285 nm)–h-BN(46 nm)–graphene–h-BN(7 nm)–vacuum. Thin film and nonlocal effects reduce $\mathrm{Re}\,q_{\mathrm{P}}$ by $\sim$5–20% from the infinite dielectric Drude model calculation (Supplementary Information). The zero-temperature random phase approximation result[48–50] was used for the graphene nonlocal conductivity $\sigma(k,\omega)$. The permittivity model of ref. 51 was used for the h-BN films, modified to include dielectric losses based on ref. 8 The damping effect from dielectric losses shown in Fig. 4 was also calculated by this method, taking phonon linewidths of 6.5 meV in-plane and 1.9 meV out-of-plane in the terminology of ref. 8, and their origin is discussed further in the Supplementary Information. In Fig. 2c,d, the colour quantity plotted is the imaginary part of the reflection coefficient of evanescent waves, evaluated at the top h-BN surface. In these figures the damping has been modified (for example, reduced dielectric loss) to enhance the visibility of modes—this does not significantly modify the mode locations.

References

1. Dean, C. R. *et al.* Boron nitride substrates for high-quality graphene electronics. *Nature Nanotech.* **5,** 722–726 (2010).
2. Geim, A. K. & Grigorieva, I. V. Van der Waals heterostructures. *Nature* **499,** 419–425 (2013).
3. Yankowitz, M. *et al.* Emergence of superlattice Dirac points in graphene on hexagonal boron nitride. *Nature Phys.* **8,** 382–386 (2012).
4. Brar, V. W. *et al.* Hybrid surface-phonon–plasmon polariton modes in graphene/monolayer h-BN heterostructures. *Nano Lett.* **14,** 3876–3880 (2014).
5. Tomadin, A., Guinea, F. & Polini, M. Generation and morphing of plasmons in graphene superlattices. *Phys. Rev. B* **90,** 161406(R) (2014).
6. Poddubny, A., Iorsh, I., Belov, P. & Kivshar, Y. Hyperbolic metamaterials. *Nature Photon.* **7,** 948–957 (2013).
7. Dai, S. *et al.* Tunable phonon polaritons in atomically thin van der Waals crystals of boron nitride. *Science* **343,** 1125–1129 (2014).
8. Caldwell, J. D. *et al.* Sub-diffractional volume-confined polaritons in the natural hyperbolic material hexagonal boron nitride. *Nature Commun.* **5,** 5221 (2014).
9. Jablan, M., Buljan, H. & Soljačić, M. Plasmonics in graphene at infrared frequencies. *Phys. Rev. B* **80,** 245435 (2009).
10. Ju, L. *et al.* Graphene plasmonics for tunable terahertz metamaterials. *Nature Nanotech.* **6,** 630–634 (2011).
11. Nikitin, A. Y., Guinea, F., García-Vidal, F. J. & Martín-Moreno, L. Edge and waveguide terahertz surface plasmon modes in graphene microribbons. *Phys. Rev. B* **84,** 161407(R) (2011).
12. Koppens, F. H. L., Chang, D. E. & García de Abajo, F. J. Graphene plasmonics: A platform for strong light-matter interactions. *Nano Lett.* **11,** 3370–3377 (2011).
13. Grigorenko, A. N., Polini, M. & Novoselov, K. S. Graphene plasmonics. *Nature Photon.* **6,** 749–758 (2012).
14. Yan, H. *et al.* Tunable infrared plasmonic devices using graphene/insulator stacks. *Nature Nanotech.* **7,** 330–334 (2012).
15. Yan, H. *et al.* Damping pathways of mid-infrared plasmons in graphene nanostructures. *Nature Photon.* **7,** 394–399 (2013).
16. Brar, V. W., Jang, M. S., Sherrott, M., Lopez, J. J. & Atwater, H. A. Highly confined tunable mid-infrared plasmonics in graphene nanoresonators. *Nano Lett.* **13,** 2541–2547 (2013).
17. Jang, M. S. *et al.* Tunable large resonant absorption in a midinfrared graphene Salisbury screen. *Phys. Rev. B* **90,** 165409 (2014).
18. Tassin, P., Koschny, T. & Soukoulis, C. M. Graphene for terahertz applications. *Science* **341,** 620–621 (2013).
19. Low, T. & Avouris, P. Graphene plasmonics for terahertz to mid-infrared applications. *ACS Nano* **8,** 1086–1101 (2014).
20. García de Abajo, F. J. Graphene plasmonics: Challenges and opportunities. *ACS Photonics* **1,** 135–152 (2014).
21. Fang, Z. *et al.* Active tunable absorption enhancement with graphene nanodisk arrays. *Nano Lett.* **14,** 299–304 (2014).
22. Wang, L. *et al.* One-dimensional electrical contact to a two-dimensional material. *Science* **342,** 614–617 (2013).
23. Fei, Z. *et al.* Gate-tuning of graphene plasmons revealed by infrared nano-imaging. *Nature* **487,** 82–85 (2012).
24. Chen, J. *et al.* Optical nano-imaging of gate-tunable graphene plasmons. *Nature* **487,** 77–81 (2012).
25. Keilmann, F. & Hillenbrand, R. Near-field microscopy by elastic light scattering from a tip. *Phil. Trans. R. Soc. Lond. A* **362,** 787–805 (2004).
26. Ocelic, N., Huber, A. & Hillenbrand, R. Pseudoheterodyne detection for background-free near-field spectroscopy. *Appl. Phys. Lett.* **89,** 101124 (2006).
27. Chen, J. *et al.* Strong plasmon reflection at nanometer-size gaps in monolayer graphene on SiC. *Nano Lett.* **13,** 6210–6215 (2013).
28. Fei, Z. *et al.* Electronic and plasmonic phenomena at graphene grain boundaries. *Nature Nanotech.* **8,** 821–825 (2013).
29. Schnell, M., Carney, P. S. & Hillenbrand, R. Synthetic optical holography for rapid nanoimaging. *Nature Commun.* **5,** 3499 (2014).
30. Alonso-González, P. *et al.* Controlling graphene plasmons with resonant metal antennas and spatial conductivity patterns. *Science* **344,** 1369–1373 (2014).
31. Gerber, J. A., Berweger, S., O'Callahan, B. T. & Raschke, M. B. Phase-resolved surface pasmon interferometry of graphene. *Phys. Rev. Lett.* **113,** 055502 (2014).
32. Principi, A. *et al.* Plasmon losses due to electron–phonon scattering: The case of graphene encapsulated in hexagonal boron nitride. *Phys. Rev. B* **90,** 165408 (2014).
33. Fei, Z. *et al.* Infrared nanoscopy of dirac plasmons at the graphene–SiO_2 interface. *Nano Lett.* **11,** 4701–4705 (2011).
34. Xue, J. *et al.* Scanning tunnelling microscopy and spectroscopy of ultra-flat graphene on hexagonal boron nitride. *Nature Mater.* **10,** 282–285 (2011).
35. Zhang, L., Fu, X. & Yang, J. Excitation of propagating plasmons in semi-infinite graphene layer by free space photons. *Commun. Theory Phys.* **61,** 751–754 (2014).
36. Johnson, P. & Christy, R. Optical constants of the noble metals. *Phys. Rev. B* **6,** 4370–4379 (1972).
37. Principi, A., Vignale, G., Carrega, M. & Polini, M. Impact of disorder on Dirac plasmon losses. *Phys. Rev. B* **88,** 121405(R) (2013).

38. Principi, A., Vignale, G., Carrega, M. & Polini, M. Intrinsic lifetime of Dirac plasmons in graphene. *Phys. Rev. B* **88,** 195405 (2013).
39. Li, Z. Q. *et al.* Dirac charge dynamics in graphene by infrared spectroscopy. *Nature Phys.* **4,** 532–535 (2008).
40. Mak, K. F. *et al.* Measurement of the optical conductivity of graphene. *Phys. Rev. Lett.* **101,** 196405 (2008).
41. Christensen, J., Manjavacas, A., Thongrattanasiri, S., Koppens, F. H. L. & García de Abajo, F. J. Graphene plasmon waveguiding and hybridization in individual and paired nanoribbons. *ACS Nano* **6,** 431–440 (2012).
42. Vakil, A. & Engheta, N. Transformation optics using graphene. *Science* **332,** 1291–1294 (2011).
43. Li, Y. *et al.* Graphene plasmon enhanced vibrational sensing of surface-adsorbed layers. *Nano Lett.* **14,** 1573–1577 (2014).
44. Nikitin, A. Y., Guinea, F., Garcia-Vidal, F. J. & Martin-Moreno, L. Surface plasmon enhanced absorption and suppressed transmission in periodic arrays of graphene ribbons. *Phys. Rev. B* **85,** 081405(R) (2012).
45. Thongrattanasiri, S., Koppens, F. H. L. & García de Abajo, F. J. Complete optical absorption in periodically patterned graphene. *Phys. Rev. Lett.* **108,** 047401 (2012).
46. Gullans, M., Chang, D., Koppens, F. H. L., García de Abajo, F. J. & Lukin, M. Single-photon nonlinear optics with graphene plasmons. *Phys. Rev. Lett.* **111,** 247401 (2013).
47. Huidobro, P. A., Nikitin, A. Y., González-Ballestero, C., Martín-Moreno, L. & García-Vidal, F. J. Superradiance mediated by graphene surface plasmons. *Phys. Rev. B* **85,** 155438 (2012).
48. Wunsch, B., Stauber, T., Sols, F. & Guinea, F. Dynamical polarization of graphene at finite doping. *New J. Phys.* **8,** 318 (2006).
49. Hwang, E. H. & Das Sarma, S. Dielectric function, screening, and plasmons in two-dimensional graphene. *Phys. Rev. B* **75,** 205418 (2007).
50. Principi, A., Polini, M. & Vignale, G. Linear response of doped graphene sheets to vector potentials. *Phys. Rev. B* **80,** 075418 (2009).
51. Cai, Y., Zhang, L., Zeng, Q., Cheng, L. & Xu, Y. Infrared reflectance spectrum of BN calculated from first principles. *Solid State Commun.* **141,** 262–266 (2007).

Author contributions

A.W. and M.B.L. performed the experiments, discussed the results and wrote the manuscript. Y.G. fabricated the samples. A.P., M.P., G.V. and M.C. provided the theory on different loss mechanisms. P.A-G. helped with measurements. K.W. and T.T. synthesized the h-BN samples. G.V., M.P., J.H., R.H. and F.H.L.K. supervised the work, discussed the results and co-wrote the manuscript. All authors contributed to the scientific discussion and manuscript revisions.

Additional information

Supplementary information is available in the online version of the paper. Reprints and permissions information is available online at www.nature.com/reprints. Correspondence and requests for materials should be addressed to F.H.L.K.

Competing financial interests

R.H. is co-founder of Neaspec GmbH, a company producing scattering-type scanning near-field optical microscope systems such as the ones used in this study. All other authors declare no competing financial interests.